Unprecedented Multifunctionality in One-Dimensional $Nb_{1-x}Ta_xS_3$ Transition Metal Trichalcogenide Alloy

Z. Hemmat[1,§], A. Ahmadiparidari[1,§], S. Wang[2,§], K. Kumar[3], M. Zepeda[4], C. Zhang[1], N. Dandu[4], S. Rastegar[1], L. Majidi[1], A. Jaradat[1], A. T. Ngo[4], K. Thornton[5], L. A. Curtiss[6], J. Cabana[3,*], Z. Huang[7,*], A. Salehi-Khojin[1,*]

[1]Department of Mechanical and Industrial Engineering, University of Illinois at Chicago, Chicago, IL, 60607, USA.

[2]Department of Physics, University of Illinois at Chicago, Chicago, IL, 60607, USA.

[3]Department of Chemistry, University of Illinois at Chicago, Chicago, IL, 60607, USA.

[4]Department of Chemical Engineering, University of Illinois at Chicago, Chicago, IL, 60607, USA.

[5]Department of Materials Science and Engineering, University of Michigan, Ann Arbor, MI 48109-2136, USA.

[6]Materials Science Division, Argonne National Laboratory, Lemont, IL 60439, USA.

[7]Department of Materials and Environmental Chemistry, Stockholm University, Stockholm, SE-106 91, Sweden.

[§]These authors contributed equally to this work.

*Corresponding authors: salehikh@uic.edu, zhehao.huang@mmk.su.se, jcabana@uic.edu

One-dimensional (1D) van der Waals materials, such as nanofibers or nanoribbons are considered as the future ultimate limit of downscaling for modern electrical and electrochemical devices. Here, for the first time, we successfully synthesize nanofibers of a solid solution transition metal trichalcogenide (TMTC), $Nb_{1-x}Ta_xS_3$, with outstanding electrical, thermal, and electrochemical characteristics rivaling the performance of the-state-of-the art materials for each application. This material shows nearly unchanged sheet resistance (~740 Ω/sq) versus bending cycles tested up to 90 cycles, stable sheet resistance in ambient conditions tested up to 60 days, remarkably high electrical breakdown current density of ~ 30 MA cm^{-2}, strong evidence of successive charge density wave (CDW) transitions, and outstanding thermal stability up to ~900 K. Additionally, this material demonstrates excellent activity and selectivity for CO_2 conversion to CO reaching ~ 350 mA cm^{-2} at – 0.8 V vs RHE with an outstanding turnover frequency number of 25 for CO formation. It also exhibits an excellent performance in a high-rate Li-air battery with the specific capacity of 3000 $mAhg^{-1}$ at a high current density of 0.3 $mAcm^{-2}$. This study uncovers the multifunctionality in 1D TMTC alloys for a wide range of high-impact applications and opens a new direction for the design of the next generation of low-dimensional materials with high performance.

One-dimensional (1D) nanomaterials such as nanowires, nanofibers, nanobelt, and nanotubes have attracted comprehensive research interest over the past few years due to their remarkable properties.[1–6] These characteristics include exotic electronic behaviors such as formation and propagation of charge density waves (CDW),[7][3,8–14] superconductivity (SC),[15–17] topological phases,[18] anisotropic electronic mobility [19] and mechanical properties,[20–22] anisotropic lattice vibration,[23] and polarized photodetection.[14,24–28] Among different 1D materials, transition-metal

trichalcogenides (TMTC) possess a unique lamellar structure made out of MX_3 layers which are weakly coupled through van der Waals (vdW) interactions and can be downscaled by mechanical or liquid phase exfoliation.[14,26,28] These processes induce strong anisotropy in the structural symmetry of the TMTCs that could result in distinctive properties along various crystalline orientations. These properties can be further tuned—or even new properties engineered-by alloying different elements at either the transition metal or the chalcogen site, since the intrinsic properties of TMTCs are anticipated to depend delicately on interactions of the transition metal or chalcogen sites within the layers.

In comparison with recent advancements in the synthesis of 2D crystals and their alloyed structures,[29–37] production of 1D nanomaterials with alloyed structures remains mainly unexplored. These structures can be synthesized by introducing heteroatom/second component into the TMTC fiber chains with an arbitrary composition ratio (x can be fine-tuned from 0 to 1) while the crystal structures can be kept in a single homogeneous phase. In this work, we report a successful synthesis, characterization and outstanding multifunctionality of 1D $Nb_{1-x}Ta_xS_3$ ($x\approx0.5$) fibers. The latter was studied through extensive electrical characterizations of individual nanofibers and thin films (I-V curves and charge density wave), long term electrical stability upon exposure to air at ambient conditions, and high temperature structural integrity as well as electrochemical catalytic properties through two distinct applications i.e. electrochemical CO_2 reduction reaction (CO2RR) in an aqueous electrolyte and Li-air battery system in an aprotic electrolyte. To further highlight how the alloying impacts the physical characteristic and performance in the above-mentioned categories, we compared the performance of this material with its end member unary metal structures of NbS_3 and TaS_3 and the state-of-the-art results in literature and discussed the nature of these improvements.

Layered $Nb_{1-x}Ta_xS_3$ nanofibers were synthesized in an evacuated ampule through chemical vapor transport (CVT). The samples were grown at 550 °C with a stoichiometric composition corresponding to x = 0.5. During a typical synthesis, the ampule was heated up to 550 °C and maintained for 5 days followed by applying a temperature gradient of 80 °C between the hot zone and cold zone. The ampule was then cooled down to room temperature and the high-quality $Nb_{1-x}Ta_xS_3$ whiskers were collected for characterization and experiments.

The morphology, composition and crystallinity of the synthesized materials were characterized with atomic-resolution scanning transmission electron microscopy (STEM), three-dimensional electron diffraction (3DED), scanning electron microscopy (SEM), energy dispersive X-ray spectroscopy (EDX), Raman spectroscopy, X-ray diffraction (XRD), Atomic force microscopy (AFM), and dynamic light scattering (DLS). **Figure S1** shows the optical photograph of the quartz ampule after the synthesis process which is covered by a dense forest of $Nb_{1-x}Ta_xS_3$ whiskers. A representative SEM image of the sample shows long belt-like nanofibers with lengths of over 500 μm (**Figures 1A and S1B-D**). The width distribution shows an average of ≈ 250-300 nm (**Figure S2**). The macroscopic compositions of the synthesized fibers are determined using SEM-EDX maps, which confirm the homogeneity of the individual fibers with the desired stoichiometry of x ≈ 0.5 (**Figures 1B**). A representative spectrum is shown in **Figure S3. Figure 1B** shows atomic force microscopy (AFM) imaging of mechanically exfoliated individual nanofibers with representative measured thickness ranging from 3-20 nm.

The high resolution high-angle annular dark-field STEM (HAADF-STEM) image observed on the nanofibers discloses lattice fringes along the fiber direction (**Figure 1C-F**). Fourier transform (FT) of the image reveals a two-dimensional (2D) lattice fringes in the image (**Figure 1E)**. Because the atoms overlap with each other, spatial resolution is insufficient to distinguish individual atoms.

Calculating the spacing based on the FT pattern, interestingly, shows a large deviation compared to those reported TaS_3 structures.[14,38–40] We therefore applied three-dimensional electron diffraction (3DED) to determine the unit cell dimension and symmetry of the nanofibers (**Supplementary Movie 1). Figures S3A-C** present the 3D reciprocal lattice reconstructed from the continuous rotation electron diffraction (cRED) data that the nanofiber was crystallized in a monoclinic crystal system. It has a face-centred unit cell with the parameters of a = 19.49 Å, b = 3.26 Å, c = 14.88 Å, and β = 112.32°. The reflection conditions can be deduced from the 2D planes (**Figure 1F and S4D-F**) as $hk0$: $h+k$=2n, $h0l$: h=2n, and $0k0$: k=2n. This leads to possible space groups C*2* (No. 5), C*m* (No. 8) and *C*2/*m* (No. 12) for the nanofibers. Using the determined unit cell, the orientation of the nanofiber in the high-resolution HAADF image can be determined. The image is viewed along the [110] direction with observed d_{004}=0.35 nm, and d_{111}=*0.33 nm*, which agree well with d_{004}=0.34 nm, and d_{111}=0.31 nm calculated from the unit cell obtained by 3DED. The unit cell of the nanofibers is closely associated with a recently reported polymorph of TaS_3.[14,38] Importantly, the diffuse scattering in **Figure 1F** (indicated by the boxes) shows that the nanofibers contains disordering of the metals in the structure.

To produce individual nanofibers for the electrical and electrochemical experiments, the synthesized alloy was suspended in isopropyl alcohol (IPA) solvent and bath-sonicated for 1 hour (inset of **Figure 2A)**. The resultant supernatant was then drop-casted onto a Si substrate to obtain nanofibers (**Figure 2A)**. The height profile distributions obtained from atomic force microscopy (AFM) on ~50 randomly selected exfoliated flakes are shown in **Figure 2B**. Dynamic light scattering (DLS) experiments from the resultant dispersion show an average width of ≈300 nm (**Figure 2B**).

Raman spectroscopy shows prominent A_g bands located at 482, 401, 383, 369, 345, 303, 273 229, 212, 167, 70 and 56 cm^{-1} (**Figure 2C**). Compared with the Raman spectra of NbS_3 and TaS_3,[25,41,42] the dominant peaks at 383 and 303 cm^{-1} appear from the (Nb-S) vibration modes. The one at 273 cm^{-1} is attributed to the major peak of TaS_3. The strong peak located at 167 cm^{-1} is corresponding to Nb–Nb stretching vibrations. In the low-frequency regime, Raman data displays a prominent peak at 56 cm^{-1}, which originates from shear displacements between adjacent layers and appears at low frequencies due to weak interlayer coupling.[25,42]

To determine the crystallinity of the $Nb_{1-x}Ta_xS_3$ alloy, XRD was performed on the bath-sonicated sample (**Figure 2D).** The majority of reflections in the diffraction pattern could be indexed with the unit cell of *C*-TaS_3 (*C*2/*m*),[14] with minor additional reflections indexable with the other existing polymorph, *P*-TaS_3 (*P*2_1/*m*) (19.53, 24.09 and 39.71 2theta).[14] The reflections did not match any of the reported polymorphs of NbS_3.[43,44] The patterns showed clear evidence of preferential orientation due to restacking of the exfoliated materials, leading to systematic absences of reflections along the *b* axis. Pawley refinement was performed with the two TaS_3 polymorphs, including preferential orientation.[14] Since only *h0l* reflections were observed, the fits only probed *a* and *c* parameters. The values were 19.92 and 15.17 Å, respectively, for the majority *C*-TaS_3, and 9.51 and 14.90 Å, respectively, for *P*-TaS_3. These values are consistent with the literature,[14,38] and, in the case of *C*-TaS_3, with the cRED results above. Nb and Ta have roughly the same ionic radius,[45] so the indexing of the pattern strongly suggests that Nb shares the Ta site in the *C*-TaS_3 lattice, again consistent with the cationic disorder inferred from cRED.

The electrical properties of this material were explored by fabricating devices on both single flakes and thin films. For single flake devices, we employed mechanical exfoliation, assisted by a dry viscoelastic polydimethylsiloxane (PDMS) stamp, to transfer the nanofibers onto a SiO_2/Si

(≈300 nm/0.5 mm) substrate for electrical measurements. Standard electron beam lithography (EBL) and nanofabrication processes were employed to pattern source–drain electrodes in the two- or four-probe configurations followed by deposition of Cr/Au (5/50 nm) as the metal electrode. Details of the electrical measurements are provided in the **Experimental Section**. A representative SEM image of a four-probe device is shown in **Figure 3A**. For all tested devices, the transport characteristics were found to be linear around zero, indicating good ohmic contacts between the $Nb_{1-x}Ta_xS_3$ nanofiber and Cr/Au electrodes (**Figure 3B**). Also, the decrease in resistance with increasing temperature, between 80-298 K, implies the semiconducting behavior of this material.

Figure 3C shows temperature-dependent resistivity in the range of 10−298 K for four-terminal $Nb_{1-x}Ta_xS_3$ devices with thickness of 17 and 21 nm, as determined from an AFM micrograph of the device (**inset of Figure 2D and Figure S5)**. The resistivity is increased from room temperature to low temperatures (10 K) with a maximum around 60 K **(Figure 3C)**. Below this temperature (~ 60 K) the resistance decreases when the temperature is decreased and then again increases below ~ 40 K. This interesting observed anomaly in the resistivity is attributed to two distinct phase transitions associated with the CDW state. [14,46,47] Overall, this trend was observed in all tested four different devices with thicknesses in the range of ~18 to 43 nm. The first and second distinct CDW transition during the resistivity measurement occurs at 55- 65 and 35-45 K temperature range, respectively, which are interpreted as successive Peierls transitions (**Figure S6**). [14,46–48] In agreement with the STEM-HAADF and XRD data, the observed resistivity trend is consistent with the CDW phase transition in the monoclinic-like TaS_3 structure.[14,46]

Next, the breakdown current density versus voltage characteristics of the 1D-$Nb_{1-x}Ta_xS_3$ nanofiber devices was tested. A summary of the breakdown parameters (i.e., breakdown voltage and current density) for all the tested devices with their width and thickness information are

provided in **Table S1**. The maximum current density that these devices were able to withstand before electrical breakdown is in the order of ~30 MA cm^{-2} (**Figure 3D**). This current density is an order of magnitude higher than typical values reported for Cu nanowires (~ 2-3 MA cm^{-2}). Even higher sustained values can be reached by encapsulating the 1D channel with h-BN as well as employing a better thermal sink as the underlying substrate.[49] The outstanding capacity to carry current observed in $Nb_{1-x}Ta_xS_3$ nanofibers can be attributed to the reduced electron scattering rate due to the crystalline structure of this 1D material. [50–52]

We also studied the electrical properties of thin film $Nb_{1-x}Ta_xS_3$ on a mica substrate. **Figure 3E** shows the SEM image of the exfoliated bundle of $Nb_{1-x}Ta_xS_3$ whiskers. Results in **Figure 3F** confirm the stability of electrical conductivity under mechanical strain. The sheet resistance remains nearly unchanged (~740 Ω/sq) versus bending cycles tested up to 90 cycles. The experiments were performed by repeatedly bending and stretching the nanofiber-coated PET sample from a diameter of 1 cm to a flattened state (inset of **Figure 3F and Figure S7**). Additional details of sample preparation are provided in the **Experimental Section**. Resistivity measurements on these thin films also verify the anomalous increases in resistance at the CDW transition temperatures of 60 K (**Figure 3G).**

The long-term electrical stability of these nanofibers at ambient condition was also tested by measuring the sheet resistance of the devices at different time intervals. Results shown in **Figure 3G** during 60 days of experiment confirm the stability of this material without any degradation. **Figure 3H** shows the thermal stability of these nanofibers measured through thermogravimetric analysis (TGA) maintained at 650 K for 3 hours with trivial weight loss of ~6% under nitrogen environment. Moreover, results show that $Nb_{1-x}Ta_xS_3$ retains its structural integrity up to ~900 K with only 6% weight loss when heated at a 10 K min^{-1} rate in N_2 Inset of **Figure 3H**). This thermal

stability exceeds those thermal stability of other 1D-TMTCs, MOF and perovskite 1D structures, which are in the range of ~ 550-800 K.[53–55]

Next, we evaluated the catalytic performance of this material toward the CO_2 electrochemical reduction reaction and in a lithium-air (Li-air) electrochemical system. The preparation of the electrodes has been discussed in supplementary material. For the CO_2 electroreduction, all experiments were carried out in a two-compartment cell where Nafion-115 was used as the membrane and 1 M KOH in an aqueous medium. The electrolyte was purged with ultra-high pure CO_2 until the pH of the solution reached ~7.6. **Figure 4A** shows the cyclic voltammetry (CV) curves for $Nb_xTa_{1-x}S_3$ and Ag NPs (known as one of the best catalysts for CO_2 conversion to CO) at a scan rate of 50 mV/s. While the current density of Ag NPs reaches to 50 mA/cm^2 at -0.8 V vs RHE, the synthesized nanofiber material shows electrochemical activity of 348 mA/cm^2 at the same potential. Online gas detection by differential electrochemical mass spectroscopy (DEMS) (**Section S8, Supporting Information**) shows a very low onset potential of -0.189 V vs RHE (inset of **Figure 4A**) while the hydrogen evolution reaction (HER) is belated until high potentials. The faradic efficiency (FE) (**Section S8, Supporting Information**) of these catalysts were also tested during one-hour chronoamperometry (CA) experiments at four different potentials. **Figure 4B** shows very high CO FE of close to 100% and 95% for -0.35V and -0.45 V vs RHE, respectively. At higher potentials, HER becomes competitive and takes up to 15% of Faradic current at -0.79 V vs RHE. Turnover numbers (TON), as a measure of number of reactions per catalyst active sites, are shown in **Figure 4C** with respect to the applied potential. $Nb_xTa_{1-x}S_3$ shows very high TON of 9.3×10^4 towards CO production (inset of **Figure 4C and Section S8, Supporting Information**). This corresponds to 25.9 s^{-1} turn over frequency (TOF, number of

reactions per site per second) while silver nanoparticles (Ag NPs) show TOF of 2.08 at -0.8 vs RHE (**Section S8, Supporting Information)**.

Furthermore, we tested the catalytic stability of $Nb_xTa_{1-x}S_3$ through a long-term chronoamperometry (CA) test. **Figure 4D** shows the catalyst operation at -0.49 V vs RHE over the course of 40 hours with continuous feed of CO_2 to avoid depletion. The catalyst shows no drop-in current implying the structural and electrochemical integrity of this material throughout the conversion process.

To assess the catalytic capability of this material for application in a Li-air battery, we also performed galvanostatic cycling test in a custom-made Swagelok battery cell, followed by the characterization of the discharge products. The battery is comprised of a Li metal foil anode (MTI Corp), a glass fiber Separator (Whatman, GF/B) and $Nb_xTa_{1-x}S_3$ nanofibers coated on GDL as a cathode. The electrolyte is comprised of 20 µl of dimethyl sulfoxide (DMSO) and 1-ethyl-3-methylimidazolium tetrafluoroborate (EMIM-BF_4) ionic liquid at a volumetric rate of 9:1 with 0.1M InI_3 redox mediator and 1M LiTFSI. **Figure 4E** shows the cycling of the battery, with a capacity of 3000 $mAhg^{-1}$ at a high current density of 0.3 $mAcm^{-2}$. Our results indicate that the battery could operate up to 80 cycles with the discharge cut-off potential of 2.5V. To characterize the discharge products, Raman spectroscopy was carried out on the discharged $Nb_xTa_{1-x}S_3$ cathodes after 20 cycles. As shown in **Figure 4F**, compared to the pristine cathode, two peaks at 250cm^{-1} and 780cm^{-1} were observed, which are characteristic peaks of Li_2O_2.[56,57] Moreover, the characteristic peaks of $Nb_xTa_{1-x}S_3$ remain unchanged, which confirms the integrity of the catalyst during the battery operation. Additionally, no Raman vibrations associated with possible side products (e.g. Li_2CO_3, LiOH) were detected. These results were further confirmed by performing in-situ differential electrochemical mass spectroscopy (DEMS) and X-ray photoelectron

spectroscopy (XPS) described in **Supplementary S8-9** .The surface structure and morphology of the cathode samples were also studied using SEM. **Figure 4G, H** shows the SEM images of the discharged and charged $Nb_xTa_{1-x}S_3$ cathode, respectively. The morphology of the Li_2O_2 discharge product shown in **Figure 4H** is in the form of toroid produced around the nanofiber structure.

To perceive the improvement and performance enhancement of $Nb_{0.5}Ta_{0.5}S_3$ through alloying, we compared this material with NbS_3 and TaS_3 as the end member structures of this material in the context of I-V curves and charge density waves, air stability of sheet resistance, break down current density, thermal stability by thermal gravimetric analysis (TGA), CO_2 reduction reaction, and Li-air battery performance. **Figures S12-13** show the transport characteristics of $Nb_{0.5}Ta_{0.5}S_3$, NbS_3 and TaS_3 nanofibers. The semiconducting behaviors of $Nb_{0.5}Ta_{0.5}S_3$, NbS_3 and TaS_3 have been demonstrated from the decrease in current with increasing temperature from 15 K to 295 K. The resistivity of $Nb_{0.5}Ta_{0.5}S_3$ nanofiber is demonstrated to be between of NbS_3 and TaS_3 nanofibers' resistivity, but closer to the NbS_3 one. **Figure S14** shows the temperature-dependent resistivity of individual nanofiber of $Nb_{0.5}Ta_{0.5}S_3$, NbS_3 and TaS_3, respectively. The anomalies are observed in the resistivity measurements of all three nanofibers, which could be attributed to distinct phase transitions associated with the charge-density-wave (CDW) state. For $Nb_{0.5}Ta_{0.5}S_3$, the two distinct CDW transitions occur at 55- 65 and 75-85 K temperature range, respectively, which are interpreted as successive Peierls transitions[14,46,47]. For NbS_3 and TaS_3 nanofiber, the anomalies in resistivity were observed at ~150 K, ~70 K and 210 K, respectively[46,58,59]. Moreover, the sheet resistances of these thin films are measured and after 40 days, the sheet resistance of $Nb_{0.5}Ta_{0.5}S_3$ only increases ~40% and remains in the same range even after 60 days, but for NbS_3 and TaS_3, the sheet resistance has been increased to five times and three orders of magnitude larger than the initial values, respectively (**Figure S14**). Relative to the only reported number in literature

for $Ti_3C_2T_z$ (2300% change over40 days), as a common member of MXene family[60,61], $Nb_{0.5}Ta_{0.5}S_3$ shows negligible sheet resistance change over time.

The breakdown current density versus voltage characteristics of the $Nb_{0.5}Ta_{0.5}S_3$, NbS_3 and TaS_3 nanofiber devices is shown in **Figure S15**. The maximum current density of $Nb_{0.5}Ta_{0.5}S_3$ is in the order of ~30 MA cm^{-2} and is among the highest found in the semiconductor nanowire and nanofiber materials such as TiS_3 (1.7 MA cm^{-2}),[55] Si NWs (0.4 MA cm^{-2}),[55] and GaN NWs (4.65 MA cm^{-2}).[62], while for TaS_3 nanofiber devices is ~ 5 MA cm^{-2} and that is ~ 4.4 MA cm^{-2} for NbS_3 device. This confirms the outstanding capacity of $Nb_{0.5}Ta_{0.5}S_3$ to carry high current density in the electronic devices. Thermal gravimetric analysis (TGA) results performed on the $Nb_{0.5}Ta_{0.5}S_3$, NbS_3 and TaS_3 are shown in **Figure S16**. Results indicate that both NbS_3 and $Nb_{0.5}Ta_{0.5}S_3$ are stable until 800K under nitrogen environment, however, TaS_3 shows ~35% weight loss denoting unstable structure stability at elevated temperatures. The structural stability of $Nb_{0.5}Ta_{0.5}S_3$ is also higher than TiS_3 (~ 25% loss at 800 K) as the only reported value among TMTC nanofibers.

Figure S17 exhibits the activity of NbS_3, TaS_3 and $Nb_{0.5}Ta_{0.5}S_3$ towards electrochemical CO_2RR. The activity of $Nb_{0.5}Ta_{0.5}S_3$ at -0.8 vs RHE (~350 mA cm^{-2}) far surpasses both NbS_3 and TaS_3 (~100 mA cm^{-2}). When compared to the state-of-the-art electrochemical catalysts renowned for their activity and selectivity for CO production listed in Table S5 such as Ag NPs (~7 mA cm^{-2}), Au NPs (~4 mA cm^{-2}), MoS_2 (~65 mA cm^{-2}), and WSe_2 (~330 mA cm^{-2}), $Nb_{0.5}Ta_{0.5}S_3$ outperforms the highest activity. We performed DFT calculations and complementary experiments to understand the source of high CO_2 activity in $Nb_{0.5}Ta_{0.5}S_3$. From our DFT calculations (**Supplementary S10**), it is deduced that the metal edges of $Nb_{0.5}Ta_{0.5}S_3$ are responsible for driving the reaction towards CO production. Briefly, we have shown that both Nb and Ta surface terminations are active towards CO_2 adsorption and reduction reaction. However, the experiments

show that while both NbS_3 and TaS_3 are close in rendering the reaction at low overpotentials they fail to reach the activity of $Nb_{0.5}Ta_{0.5}S_3$ at higher overpotentials. We attribute this higher activity of $Nb_{0.5}Ta_{0.5}S_3$ at higher potentials to higher oxidation resistance of this material which is of utmost importance especially at high overpotentials with higher rates of reaction. The high stability of $Nb_{0.5}Ta_{0.5}S_3$ was confirmed by performing XRD on pristine and used cathodes after chronoamperometry experiments (**Figures S18-20**). This stability is derived from configurational entropy reinforcing the structure stability that makes the $Nb_{0.5}Ta_{0.5}S_3$ more durable against oxidation at higher overpotential which is not the case for neither NbS_3 nor TaS_3.

The electrochemical performance of $NbTaS_3$ in an Li-air battery system was also investigated and compared to NbS_3 and TaS_3 (**Figure S22**). Our results show that at a high current density of 0.3 mA cm^{-2}, $NbTaS_3$ upholds 80 cycles of charge and discharge while this number is reduced to 50 and 40 for TaS_3 and NbS_3, respectively. The specific capacity of $Nb_{0.5}Ta_{0.5}S_3$ based Li-air battery system (3000 mAh g^{-1}) outperforms most of catalysts listed in Table S6 including MoS_2 (1000 mAh g^{-1}) and carbon nanotube (800 mAh g^{-1}) that could withstand over 50 cycles of operation at the current density of >0.1 mA cm^{-2}.

In summary, we successfully synthesized and characterized a binary TMTC alloy of $Nb_{1-x}Ta_xS_3$. It was uncovered that this material exhibits multifunctional electrical, thermal, and electrochemical properties rivaling the performance of the state-of-the-art materials for each application. It was also revealed that 1D TMTCs could be excellent candidate materials for high performance electronic and electrochemical applications. Further studies are needed to exploit the vast compositional space and explore the role of alloying in tuning their intrinsic properties. It is expected that TMTCs' anisotropic interfacial thermodynamics and kinetics, as well as the intermediate species that are involved, play key roles in the rate of growth and morphologies of

the resulting products. The fundamental understanding of these underlying physics and chemistry of TMTCs will be critical in unlocking the full potential of the material, which will be a focus of a future study.

Experimental Section:

Chemical Vapor Transport (CVT) of TMTC alloy: In the CVT synthesis process, growth reaction occurs in sealed ampoules. First, the quartz ampoules are thoroughly cleaned using diluted HF followed by rinsing with distilled water and annealing at 1050 °C for 5 h. This cleaning process is a necessary step as it removes any contamination which interferes with the quality of the synthesized crystals. High-purity chemical elements (>99.99% trace metals basis) are mixed in desired stoichiometric proportions and sealed under high vacuum ($<10^{-5}$ Torr) in the ampule. The sealed quartz is placed into a two-zone furnace system for the vapor transport growth process. During the synthesis process, first both zones of the furnace are heated up to the growth temperature of 550 °C and then a temperature gradient of 80 °C is established between the hot zone (T_{hot}) and the cold zone (T_{cold}). The furnace is maintained at this temperature for one week and then gradually cooled down to room temperature. Finally, high crystalline materials are collected from the quartz ampules.

Characterization techniques:
The high-resolution scanning transmission electron microscopy (STEM) high-angle annular dark-field (HAADF) images were recorded on an aberration-corrected Thermo Fisher Themis Z transmission electron microscope. Samples for transmission electron microscopy observation were dispersed in IPA. A droplet of the suspension was transferred onto a carbon-coated copper grid. The instrument was operated at an acceleration voltage of 300 kV. Three-dimensional electron diffraction (3DED) data was collected using continuous rotation (cRED) protocol. A single-tilt tomography sample holder was used for the data collection, which was performed on a JEOL JEM2100 microscope operated at 200 kV with a Timepix hybrid detector QTPX-262k (Amsterdam Sci. Ins.). Scanning Electron Microscopy (SEM) characterization was performed using the Raith e-LiNE plus ultra-high-resolution electron beam lithography (EBL) system. Imaging was performed by an acceleration voltage (EHT) of 12 kV.

The SEM-EDX measurements were carried out with FEI Quanta 650 ESEM integrated with the Oxford AZtec EDS and EBSD systems. The data were obtained in high vacuum condition with excellent beam stability.

Raman data were obtained with a HORIBA LabRAM HR Evolution confocal Raman microscope equipped with a Horiba Andor detector and 633 nm laser source for excitation. The measurements were performed in ambient conditions and at room temperature.

Thermal analyses were performed using a Q5000 TA instrument under Nitrogen gas. TGA experiments were conducted using a 10 K min^{-1} ramp rate in a Pt pan.

X-ray diffraction (XRD) was conducted on a Bruker D8 Advance (40 kV, 40 mA) using a Cu Kα (λavg= 1.5418 Å). The diffraction pattern was recorded from 7.5° to 80° (2θ).

Dynamic Light Scattering (DLS) measurements were performed using the Malvern Zetasizer Nano ZLS 380 system equilibrated at 25 °C for 60 s. The instrument equipped with a 10 mW, 633 nm semiconductor laser.

Atomic force microscopy (AFM) topography images were obtained using Bruker Dimension Icon AFM with ScanAsyst-tapping mode.

Exfoliation of TMTC alloy nanofibers (NFs): TMDC nanofibers (NFs) were synthesized using a bath-sonicated exfoliation method in isopropyl alcohol (IPA) solvent. The sonication was carried out for one hour and the resultant supernatant was collected for further experiments. For the mechanical exfoliation, a polydimethylsiloxane (PDMS) stamp is attached to the TMTC material and then slowly peeled off and then transferred to the desired substrate.

Electrical and mechanical measurements: The $Nb_{1-x}Ta_xS_3$ devices were loaded in a cryogenic probe station under high vacuum environment (chamber pressure = 10^{-8} to 10^{-7} Torr) for electrical measurements. Keithley 2612A System Source Meter was used for applying power to test the Current-voltage (I_{DS}-V_{DS}) and resistivity characteristics. For the mechanical test, the exfoliated solution was deposited on a PMMA-coated polyethylene terephthalate (PET) substrate. The widely available PET is a plastic material used as a substrate for flexible electronics. We repeatedly bent and stretched the $Nb_{1-x}Ta_xS_3$-coated PET for 90 cycles to record the stability of the sheet resistance versus bending cycles. During this mechanical cycling, the sample was bent from a flat state to a radius of curvature of 5mm by using two micromanipulators in a probe station.

Acknowledgements
The work of A.S.-K., Z.H., A.A.-P., and S.W was supported by National Science Foundation (NSF) DMREF 1729420. The work of M.Z., N.D., A.T.N, L.A.C., C.Z., L. M. and A.S.-K., C.Z., L. M. and A.S.-K. was supported by Department of Energy, Office of Energy Efficiency and Renewable Energy, Vehicle Technologies Office. The work of K.K. and J.C. was supported by National Science Foundation (NSF) through grant CBET-1800357. Z. Huang acknowledges the Swedish Research Council (VR, 2016-04625) and the Swedish Research Council Formas (2020-00831) for support. The authors acknowledge the use of the Nanotechnology Core Facility and Electron Microscopy Core of UIC's Research Resources Center. This work made use of the Pritzker Nanofabrication Facility at the University of Chicago and the EPIC and Keck-II facility of Northwestern University's NUANCE Center (DMR-1720139 and NSF ECCS-1542205).

Conflict of Interest
The authors declare no conflict of interest.

Authors Contribution
A.S.-K. led the material synthesis and electrochemical/thermal/electronic experiments. J.C. led the XRD characterization and analysis. Z. Huang led the atomic-resolution STEM characterization. Z.H synthesized the TMTC alloys and performed EDX and SEM characterizations. A.A.-P. performed the electrochemical and TGA experiments. Z.H. and S.W. performed AFM, Raman, device nanofabrication and electrical measurements. C.Z. and S.R. performed battery test. K.K performed XRD. L.M. carried out DLS experiment. M.Z., N. D., A. T. N., L. A. C. performed density functional calculations. All authors contributed to the write up of the manuscript.

Keywords:
Transition metal chalcogenides, alloy, one-dimensional materials, charge density wave, current density, CO_2 reduction, lithium air battery, thermal stability.

References:

[1] C. Jin, E. C. Regan, A. Yan, M. Iqbal Bakti Utama, D. Wang, S. Zhao, Y. Qin, S. Yang, Z. Zheng, S. Shi, K. Watanabe, T. Taniguchi, S. Tongay, A. Zettl, F. Wang, *Nature* **2019**, *567*, 76.
[2] A. Aljarb, J.-H. Fu, C.-C. Hsu, C.-P. Chuu, Y. Wan, M. Hakami, D. R. Naphade, E. Yengel, C.-J. Lee, S. Brems, T.-A. Chen, M.-Y. Li, S.-H. Bae, W.-T. Hsu, Z. Cao, R. Albaridy, S. Lopatin, W.-H. Chang, T. D. Anthopoulos, J. Kim, L.-J. Li, V. Tung, *Nat. Mater.* **2020**, *19*, 1300.
[3] J. D. Cain, S. Oh, A. Azizi, S. Stonemeyer, M. Dogan, M. Thiel, P. Ercius, M. L. Cohen, A. Zettl, *Nano Lett.* **2021**, *21*, 3211.
[4] Y. Bai, L. Zhou, J. Wang, W. Wu, L. J. McGilly, D. Halbertal, C. F. B. Lo, F. Liu, J. Ardelean, P. Rivera, N. R. Finney, X.-C. Yang, D. N. Basov, W. Yao, X. Xu, J. Hone, A. N. Pasupathy, X.-Y. Zhu, *Nat. Mater.* **2020**, *19*, 1068.
[5] E. A. Stach, *Nat. Mater.* **2019**, *18*, 4.
[6] H. Sun, Y. Zhang, J. Zhang, X. Sun, H. Peng, *Nat. Rev. Mater.* **2017**, *2*, 17023.
[7] Y. Jin, X. Li, J. Yang, *Phys. Chem. Chem. Phys.* **2015**, *17*, 18665.
[8] M. Randle, A. Lipatov, A. Kumar, C.-P. Kwan, J. Nathawat, B. Barut, S. Yin, K. He, N. Arabchigavkani, R. Dixit, T. Komesu, J. Avila, M. C. Asensio, P. A. Dowben, A. Sinitskii, U. Singisetti, J. P. Bird, *ACS Nano* **2019**, *13*, 803.
[9] S. G. Zybtsev, V. Y. Pokrovskii, V. F. Nasretdinova, S. V. Zaitsev-Zotov, V. V Pavlovskiy, A. B. Odobesco, W. W. Pai, M.-W. Chu, Y. G. Lin, E. Zupanič, H. J. P. van Midden, S. Šturm, E. Tchernychova, A. Prodan, J. C. Bennett, I. R. Mukhamedshin, O. V. Chernysheva, A. P. Menushenkov, V. B. Loginov, B. A. Loginov, A. N. Titov, M. Abdel-Hafiez, *Phys. Rev. B* **2017**, *95*, 035110.
[10] S. G. Zybtsev, V. Y. Pokrovskii, V. F. Nasretdinova, S. V. Zaitsev-Zotov, *Appl. Phys. Lett.* **2009**, *94*, 152112.
[11] J. O. Island, A. J. Molina-Mendoza, M. Barawi, R. Biele, E. Flores, J. M. Clamagirand, J. R. Ares, C. Sánchez, H. S. J. van der Zant, R. D'Agosta, I. J. Ferrer, A. Castellanos-Gomez, *2D Mater.* **2017**, *4*, 022003.
[12] K. Inagaki, S. Tanda, *Phys. Rev. B* **2018**, *97*, 115432.
[13] J. Yang, Y. Q. Wang, R. R. Zhang, L. Ma, W. Liu, Z. Qu, L. Zhang, S. L. Zhang, W. Tong, L. Pi, W. K. Zhu, C. J. Zhang, *Appl. Phys. Lett.* **2019**, *115*, 033102.
[14] C. C. Mayorga-Martinez, Z. Sofer, J. Luxa, Š. Huber, D. Sedmidubský, P. Brázda, L. Palatinus, M. Mikulics, P. Lazar, R. Medlín, M. Pumera, *ACS Nano* **2018**, *12*, 464.
[15] S. J. Denholme, A. Yukawa, K. Tsumura, M. Nagao, R. Tamura, S. Watauchi, I. Tanaka, H. Takayanagi, N. Miyakawa, *Sci. Rep.* **2017**, *7*, 45217.
[16] E. Garnett, L. Mai, P. Yang, *Chem. Rev.* **2019**, *119*, 8955.
[17] A. P. Petrović, D. Ansermet, D. Chernyshov, M. Hoesch, D. Salloum, P. Gougeon, M. Potel, L. Boeri, C. Panagopoulos, *Nat. Commun.* **2016**, *7*, 12262.
[18] K.-H. Jin, F. Liu, *Nanoscale* **2020**, *12*, 14661.
[19] J. O. Island, M. Barawi, R. Biele, A. Almazán, J. M. Clamagirand, J. R. Ares, C. Sánchez,

H. S. J. Van Der Zant, J. V Álvarez, R. D. Agosta, I. J. Ferrer, A. Castellanos-gomez, **2015**, 2595.
[20] J. Kang, H. Sahin, F. M. Peeters, *Phys. Chem. Chem. Phys.* **2015**, *17*, 27742.
[21] M. Li, J. Dai, X. C. Zeng, *Nanoscale* **2015**, *7*, 15385.
[22] J. Kang, H. Sahin, H. D. Ozaydin, R. T. Senger, F. M. Peeters, *Phys. Rev. B* **2015**, *92*, 75413.
[23] A. Lipatov, M. J. Loes, H. Lu, J. Dai, P. Patoka, N. S. Vorobeva, D. S. Muratov, G. Ulrich, B. Kästner, A. Hoehl, G. Ulm, X. C. Zeng, E. Rühl, A. Gruverman, P. A. Dowben, A. Sinitskii, *ACS Nano* **2018**, *12*, 12713.
[24] K. Wu, E. Torun, H. Sahin, B. Chen, X. Fan, A. Pant, D. P. Wright, T. Aoki, F. M. Peeters, E. Soignard, S. Tongay, **2016**, 1.
[25] K. Wu, B. Chen, H. Cai, M. Blei, J. Bennett, S. Yang, D. Wright, Y. Shen, S. Tongay, **2017**, DOI 10.1021/acs.jpcc.7b10263.
[26] K. Wu, M. Blei, B. Chen, L. Liu, H. Cai, C. Brayfield, D. Wright, H. Zhuang, S. Tongay, *Adv. Mater.* **2020**, *32*, 1.
[27] S. Yang, M. Wu, W. Shen, L. Huang, S. Tongay, K. Wu, B. Wei, Y. Qin, Z. Wang, C. Jiang, C. Hu, *ACS Appl. Mater. Interfaces* **2019**, *11*, 3342.
[28] S. Hou, Z. Guo, J. Yang, Y. Liu, W. Shen, C. Hu, S. Liu, H. Gu, Z. Wei, *Small* **2021**, *n/a*, 2100457.
[29] S. Wang, J. Cavin, Z. Hemmat, K. Kumar, A. Ruckel, L. Majidi, H. Gholivand, R. Dawood, J. Cabana, N. Guisinger, R. F. Klie, F. Khalili-Araghi, R. Mishra, A. Salehi-Khojin, *Adv. Funct. Mater.* **2020**, *30*, 2004912.
[30] Z. Hemmat, J. Cavin, A. Ahmadiparidari, A. Ruckel, S. Rastegar, S. N. Misal, L. Majidi, K. Kumar, S. Wang, J. Guo, R. Dawood, F. Lagunas, P. Parajuli, A. T. Ngo, L. A. Curtiss, S. B. Cho, J. Cabana, R. F. Klie, R. Mishra, A. Salehi-Khojin, *Adv. Mater.* **2020**, *32*, 1907041.
[31] J. Zhou, J. Lin, X. Huang, Y. Zhou, Y. Chen, J. Xia, H. Wang, Y. Xie, H. Yu, J. Lei, D. Wu, F. Liu, Q. Fu, Q. Zeng, C.-H. Hsu, C. Yang, L. Lu, T. Yu, Z. Shen, H. Lin, B. I. Yakobson, Q. Liu, K. Suenaga, G. Liu, Z. Liu, *Nature* **2018**, *556*, 355.
[32] J. Park, M. S. Kim, B. Park, S. H. Oh, S. Roy, J. Kim, W. Choi, *ACS Nano* **2018**, *12*, 6301.
[33] S. Susarla, A. Kutana, J. A. Hachtel, V. Kochat, A. Apte, R. Vajtai, J. C. Idrobo, B. I. Yakobson, C. S. Tiwary, P. M. Ajayan, *Adv. Mater.* **2017**, *29*, 1.
[34] Y. Chen, D. O. Dumcenco, Y. Zhu, X. Zhang, N. Mao, Q. Feng, M. Zhang, J. Zhang, P.-H. Tan, Y.-S. Huang, L. Xie, *Nanoscale* **2014**, *6*, 2833.
[35] M. Falmbigl, Z. Hay, J. Ditto, G. Mitchson, D. C. Johnson, *J. Mater. Chem. C* **2015**, *3*, 12308.
[36] P. Yu, J. Lin, L. Sun, Q. L. Le, X. Yu, G. Gao, C.-H. Hsu, D. Wu, T.-R. Chang, Q. Zeng, F. Liu, Q. J. Wang, H.-T. Jeng, H. Lin, A. Trampert, Z. Shen, K. Suenaga, Z. Liu, *Adv. Mater.* **2017**, *29*, 1603991.
[37] S. Tongay, D. S. Narang, J. Kang, W. Fan, C. Ko, A. V. Luce, K. X. Wang, J. Suh, K. D. Patel, V. M. Pathak, J. Li, J. Wu, *Appl. Phys. Lett.* **2014**, *104*, 1.
[38] A. Meerschaut, L. Guemas, J. Rouxel, *J. Solid State Chem.* **1981**, *36*, 118.
[39] R. A. Gardner, M. Vlasse, A. Wold, *Inorg. Chem.* **1969**, *8*, 2784.
[40] S. A. Sunshine, J. A. Ibers, *Acta Crystallogr. Sect. C* **1987**, *43*, 1019.
[41] C. Sourisseau, R. Cavagnat, M. Fouassier, P. Maraval, *J. Raman Spectrosc.* **1990**, *21*, 337.

[42] V. E. Fedorov, S. B. Artemkina, E. D. Grayfer, N. G. Naumov, Y. V. Mironov, A. I. Bulavchenko, V. I. Zaikovskii, I. V. Antonova, A. I. Komonov, M. V. Medvedev, *J. Mater. Chem. C* **2014**, *2*, 5479.
[43] J. Rijnsdorp, F. Jellinek, *J. Solid State Chem.* **1978**, *25*, 325.
[44] E. Zupanič, H. J. P. van Midden, M. A. van Midden, S. Šturm, E. Tchernychova, V. Y. Pokrovskii, S. G. Zybtsev, V. F. Nasretdinova, S. V Zaitsev-Zotov, W. T. Chen, W. W. Pai, J. C. Bennett, A. Prodan, *Phys. Rev. B* **2018**, *98*, 174113.
[45] R. D. Shannon, *Acta Crystallogr. Sect. A* **1976**, *32*, 751.
[46] C. Roucau, R. Ayroles, P. Monceau, L. Guemas, A. Meerschaut, J. Rouxel, *Phys. Status Solidi* **1980**, *62*, 483.
[47] S. Sridhar, D. Reagor, G. Gruner, *Phys. Rev. Lett.* **1985**, *55*, 1196.
[48] W. Shi, B. J. Wieder, H. L. Meyerheim, Y. Sun, Y. Zhang, Y. Li, L. Shen, Y. Qi, L. Yang, J. Jena, P. Werner, K. Koepernik, S. Parkin, Y. Chen, C. Felser, B. A. Bernevig, Z. Wang, *Nat. Phys.* **2021**, *17*, 381.
[49] M. A. Stolyarov, G. Liu, M. A. Bloodgood, E. Aytan, C. Jiang, R. Samnakay, T. T. Salguero, D. L. Nika, S. L. Rumyantsev, M. S. Shur, K. N. Bozhilov, A. A. Balandin, *Nanoscale* **2016**, *8*, 15774.
[50] H. Li, G. Lu, Y. Wang, Z. Yin, C. Cong, Q. He, L. Wang, F. Ding, T. Yu, H. Zhang, *Small* **2013**, *9*, 1974.
[51] L. Yang, M. P. Gordon, A. K. Menon, A. Bruefach, K. Haas, M. C. Scott, R. S. Prasher, J. J. Urban, *Sci. Adv.* **2021**, *7*, eabe6000.
[52] Y. Xia, P. Yang, Y. Sun, Y. Wu, B. Mayers, B. Gates, Y. Yin, F. Kim, H. Yan, *Adv. Mater.* **2003**, *15*, 353.
[53] Z. Yuan, C. Zhou, Y. Tian, Y. Shu, J. Messier, J. C. Wang, L. J. van de Burgt, K. Kountouriotis, Y. Xin, E. Holt, K. Schanze, R. Clark, T. Siegrist, B. Ma, *Nat. Commun.* **2017**, *8*, 14051.
[54] F. González Chávez, H. I. Beltrán, *New J. Chem.* **2021**, DOI 10.1039/D0NJ04055J.
[55] A. J. Molina-Mendoza, J. O. Island, W. S. Paz, J. M. Clamagirand, J. R. Ares, E. Flores, F. Leardini, C. Sánchez, N. Agraït, G. Rubio-Bollinger, H. S. J. van der Zant, I. J. Ferrer, J. J. Palacios, A. Castellanos-Gomez, *Adv. Funct. Mater.* **2017**, *27*, 1.
[56] D. Zhai, H.-H. Wang, K. C. Lau, J. Gao, P. C. Redfern, F. Kang, B. Li, E. Indacochea, U. Das, H.-H. Sun, H.-J. Sun, K. Amine, L. A. Curtiss, *J. Phys. Chem. Lett.* **2014**, *5*, 2705.
[57] F. S. Gittleson, K. P. C. Yao, D. G. Kwabi, S. Y. Sayed, W.-H. Ryu, Y. Shao-Horn, A. D. Taylor, *ChemElectroChem* **2015**, *2*, 1446.
[58] S. G. Zybtsev, V. Y. Pokrovskii, V. F. Nasretdinova, S. V. Zaitsev-Zotov, V. V. Pryadun, E. S. Kozlyakova, O. S. Volkova, A. N. Vasiliev, W. W. Pai, D. Starešinić, *Phys. Rev. B* **2019**, *99*, 235155.
[59] K. Hasegawa, A. Maeda, S. Uchida, S. Tanaka, *Phys. B+C* **1983**, *117–118*, 599.
[60] M. Mariano, O. Mashtalir, F. Q. Antonio, W.-H. Ryu, B. Deng, F. Xia, Y. Gogotsi, A. D. Taylor, *Nanoscale* **2016**, *8*, 16371.
[61] T. Habib, X. Zhao, S. A. Shah, Y. Chen, W. Sun, H. An, J. L. Lutkenhaus, M. Radovic, M. J. Green, *npj 2D Mater. Appl.* **2019**, *3*, 8.
[62] J. Qu, R. Wang, Y. Sun, I. Shih, Z. Mi, X. Liu, *Appl. Phys. Lett.* **2018**, *113*, 193103.

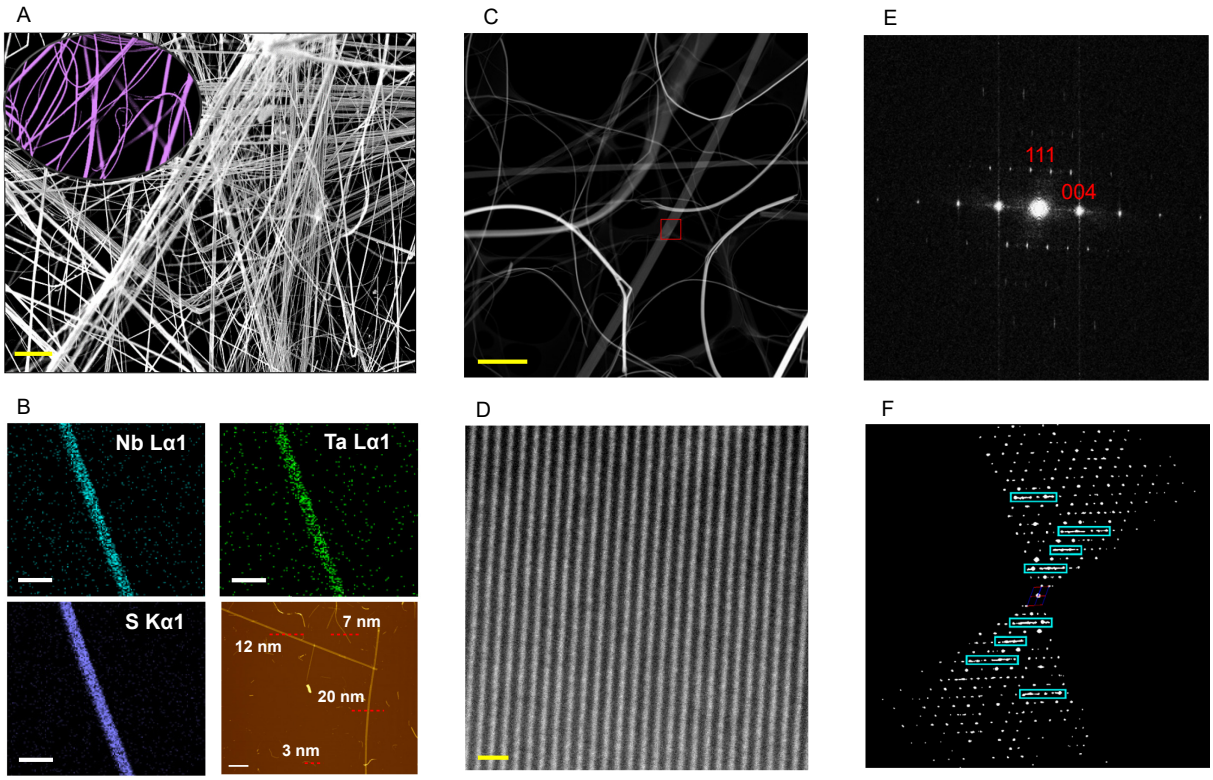

Figure 1. Summary of characterization of 1D-$Nb_{1-x}Ta_xS_3$ alloy. **(A)** SEM image of long belt-like $Nb_{1-x}Ta_xS_3$ nanofibers (scale bar: 50 μm). **(B)** SEM-EDX elemental maps obtained from individual fibers (scale bar: 2 μm) and a typical AFM topography image of bath-sonicated fibers with the heights of 3 to 20 nm (scale bar: 5 μm). **(C)** HAADF STEM image of the $Nb_{1-x}Ta_xS_3$ nanofibers (scale bar: 200 nm). **(D)** High-resolution HAADF STEM image of the nanofiber viewed along the [110] direction, showing clear lattice fringes (scale bar: 1 nm). **(E)** Fourier transforms of the image. **(F)** 2D slice cuts from the reconstructed 3D reciprocal lattice show the *h0l* plane. Diffused scattering can be observed in the data, which indicates disordered structure of $Nb_{1-x}Ta_xS_3$ nanofibers.

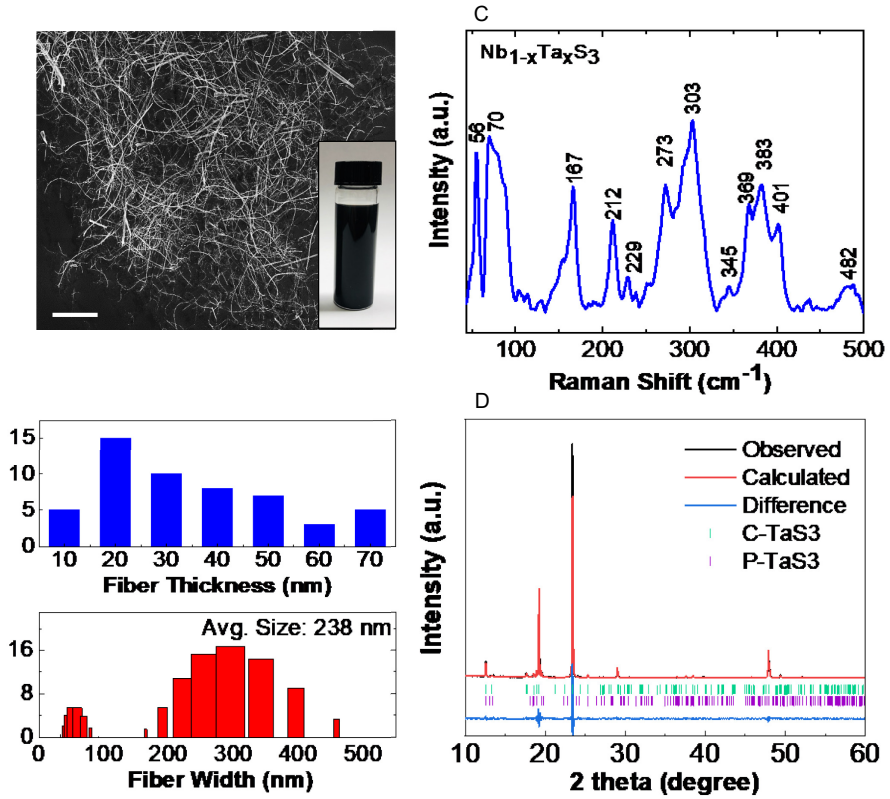

Figure 2. Summary of characterization of 1D-$Nb_{1-x}Ta_xS_3$ nanofibers. **(A)** SEM image of drop casted solution on Si Substrate (scale bar: 5 µm). Inset shows dispersions of exfoliated $Nb_{1-x}Ta_xS_3$ nanofibers in IPA solvent. **(B)** AFM frequency distribution obtained from ~50 randomly selected exfoliated fibers and size distribution from DLS measurements for $Nb_{1-x}Ta_xS_3$ alloy. **(C)** Raman characteristics of TMTC alloy at ambient conditions excited by 633 nm laser. **(D)** Pawley refinement of the XRD patterns obtained from 1D-$Nb_{1-x}Ta_xS_3$ nanofibers.

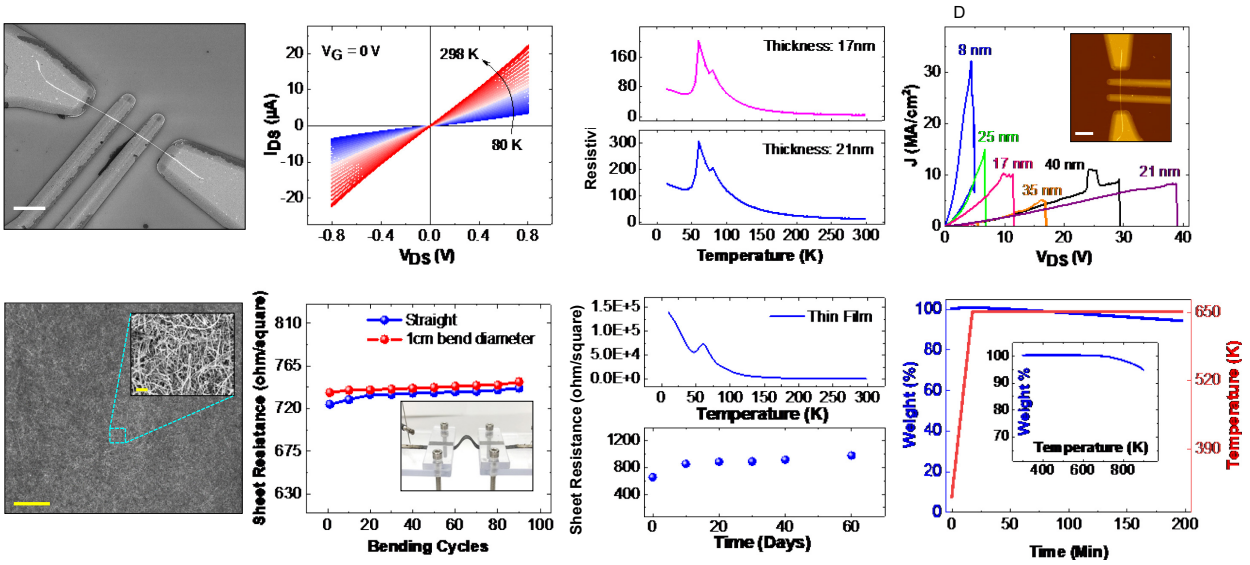

Figure 3. Electrical properties and thermal stability of $Nb_{1-x}Ta_xS_3$ nanofibers. **(A)** SEM image of four-probe device fabricated on exfoliated $Nb_{1-x}Ta_xS_3$ nanofiber (scale bar: 4 μm). **(B)** Current–voltage (I_{DS}–V_{DS}) characteristics of four-probe device at 80–298 K temperatures range. **(C)** Temperature dependence of resistivity of $Nb_{1-x}Ta_xS_3$ exfoliated nanofibers. **(D)** Measured current density versus voltage characteristics of $Nb_{1-x}Ta_xS_3$ nanofibers approaching high breakdown current density of 30 MA cm^{-2}. Thickness of individual tested nanofibers are shown by different colors. Inset shows an AFM image of a four-probe device (Scale bar: 5 μm). **(E)** SEM image of the exfoliated bundle of $Nb_{1-x}Ta_xS_3$ whiskers (scale bar: 200 μm). Inset magnifies the area shown by square (scale bar: 5 μm). **(F)** Sheet resistance versus bending cycles for $Nb_{1-x}Ta_xS_3$ nanofibers. Inset shows PET substrate covered with the $Nb_{1-x}Ta_xS_3$ whiskers after ~90 cycles. **(G)** Temperature dependent resistivity of thin film $Nb_{1-x}Ta_xS_3$ and air-stability of sheet resistance at ambient condition versus time. **(H)** TGA curve for annealing the $Nb_{1-x}Ta_xS_3$ nanofibers at 650 K for 3 hours. Inset shows TGA curves at a 10 K/min from room temperature to 900K.

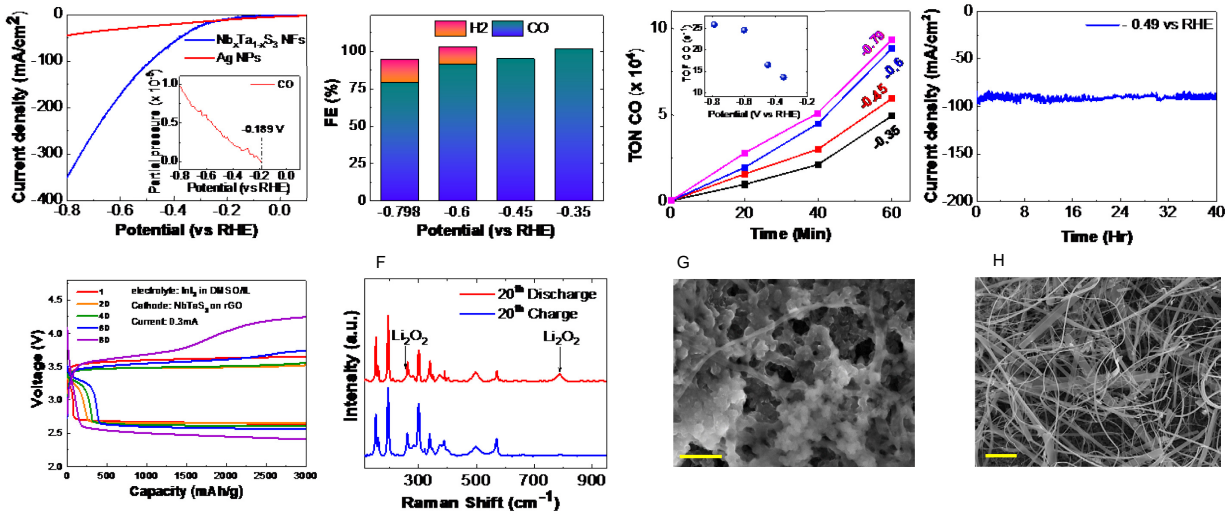

Figure 4. Electrochemical CO_2 conversion and Li-air battery experiments using $Nb_{1-x}Ta_xS_3$ nanofibers-based cathodes. **(A)** CV test at 50mV/s scan rate for Ag nanoparticles (red) and $NbTaS_3$ nanofibers (Blue). The inset shows the onset potential of CO production measured by online DEMS at a scan rate of 1 mV/sec. **(B)** Faradic efficiency (FE) towards production of CO and H_2 from CA experiments at four different potentials. **(C)** Turnover number over an hour of CA experiments showing the activity of $NbTaS_3$ catalyst with the TOF in the inset. **(D)** Catalyst stability test over 40 hours at the potential of – 0.49 V vs RHE. **(E)** Li-air battery cycling performance utilizing $Nb_xTa_{1-x}S_3$ catalyst. **(F)** Raman spectroscopy of the cathode after 20th discharge and charge cycle. SEM image of the cathode surface after **(G)** 20th discharge and **(H)** 20th charge cycle (scale bars: 1 μm).

bvc